Relaxation Dynamics and Structural Characterization of Organic Nanoparticles with Enhanced Emission

Chetan Jagdish Bhongale, Chih-Wei Chang, Chi-Shen Lee, Eric Wei-Guang Diau,* and Chain-Shu Hsu

Department of Applied Chemistry, Institute of Molecular Science and Center for Interdisciplinary Molecular Science, National Chiao Tung University, Hsinchu, Taiwan 30010

Received: January 13, 2005; In Final Form: May 19, 2005

With a reprecipitation method, we prepared fluorescent organic nanoparticles of 1,4-di[(*E*)-2-phenyl-1-propenyl]-benzene (PPB) that feature weak emission in solution but exhibit blue-shifted absorption and strong emission as aggregates. Picosecond fluorescent transients of these PPB nanoparticles showed biexponential decay, described with a consecutive kinetic model involving two emissive states. X-ray diffraction patterns of PPB nanocrystals indicate long-range packing structures of two types, one the same as in a single crystal and the other not yet determined. PPB molecules in a crystal show an arrangement of a herringbone type with three benzene rings in a PPB unit being nearly planar and two methyl groups of the unit pointing along the same direction, in contrast to the twisted structure of an isolated PPB molecule. Fluorescence transients of PPB on a femtosecond scale indicate an efficient channel for isomerization that is activated for free PPB in solution but inhibited in PPB forming nanoparticles, demonstrating the significance of molecular geometry and twisting motions that affect the relaxation dynamics in the excited state. The versatile techniques combined in this work provide strong evidence to improve our understanding of optical properties in organic nanoparticles dependent on size.

Introduction

Organic nanoparticles have attracted much research interest because their special properties lie between the properties of molecules and those of bulk materials.[1] The electronic properties of organic nanoparticles differ fundamentally from those of inorganic ones[2] because of weak intermolecular forces accompanying interactions of van der Waals type or hydrogen bonding.[3] Organic nanocrystals allow much increased variability and flexibility in synthesis of materials, preparation of nanoparticles, and investigation of their physicochemical properties such as luminescence[4] or large nonlinear optical efficiency;[5] they are thus expected to serve as novel functional materials in electronics and photonics.[6] From a fundamental point of view, organic nanoparticles are fascinating because their optical properties on absorption and emission depend on size.[7−10] Nakanashi and co-workers[7] pioneered investigation of this subject, particularly focusing on fabrication of nanocrystals and characterization of perylene[7a−d] and other organic systems.[6b,7e−g] According to an investigation of nanoparticles of pyrazoline derivatives,[8] the emitted color can be tuned with either the particle size or the excitation wavelength. Enhanced emission due to aggregation has been reported for organic systems including CN-MBE,[9] *p*-BSP,[10] a silole derivative,[11] and conjugated polymers.[12]

This feature of aggregation-induced emission is remarkable because intermolecular vibronic interactions generally induce nonradiative deactivation that produces quenching of emission.[13] Characterization of organic nanoparticles has nevertheless provided strong evidence for this enhanced emission, even if the free molecule itself is almost nonfluorescent in dilute solution. For instance, the weak fluorescence intensity of CN-MBE in dilute solution was found to increase greatly when nanoparticles were produced in mixtures of water and THF;[9] moreover, UV spectral features of CN-MBE nanoparticles in absorption are red-shifted with respect to those of molecules in dilute solution. Computational simulation indicates that isolated CN-MBE molecules are twisted in their biphenyl units, whereas the corresponding nanoparticles were speculated to be nearly planar; the enhanced fluorescence of CN-MBE nanoparticles was thus proposed to reflect both intra- and intermolecular effects.[9] In contrast, the planar DPST molecule constitutes an example of fluorescence quenching in nanoparticles with blue-shifted absorption.[9] According to a general rule based on a molecular exciton model,[14,15] a parallel alignment of transition dipole moments, known as H-aggregation, shifts absorption to the blue and diminishes emitted intensity, whereas head-to-tail alignment, J-aggregation, shifts absorption to the red and enhances the emission. The observed enhanced fluorescence of CN-MBE and fluorescence quenching in DPST is then readily explicable according to this exciton model as the former existing in J-aggregation and the latter in H-aggregation.

Here we report fluorescent organic nanoparticles of 1,4-di-[(*E*)-2-phenyl-1-propenyl]benzene (PPB) in a new class that

CHART 1: Chemical Structures of PPB and DSB

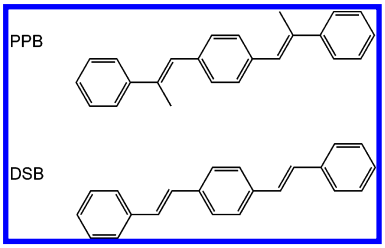

* Corresponding author. E-mail: diau@mail.ac.nctu.edu.tw. Fax: (886)-03-572-3764.

10.1021/jp0502297 CCC: $30.25
Published on Web 06/25/2005

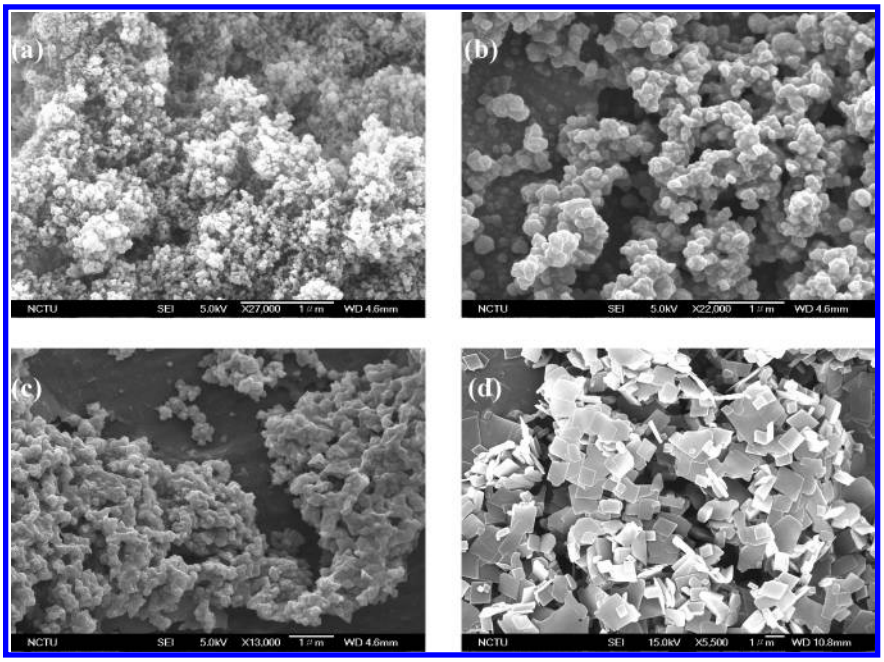

Figure 1. SEM images of PPB nanocrystals showing the size as average diameters, (a) 50, (b) 150, (c) 300 nm, and (d) ~1 μm obtained from suspensions of nanoparticles contained for 65, 70, 75, and 80% volume fractions of water added to THF, respectively.

belongs to the family of oligophenylenevinylenes (OPV) with two methyl groups added to the 1,4-distyrylbenzene (DSB) skeleton (Chart 1). We observed that fluorescent emission from PPB nanoparticles is intense, whereas PPB itself is nonfluorescent in dilute solution, analogous to the enhanced emission observed for CN-MBE.[9] In contrast, despite the similarity of chemical structure between PPB and DSB, free DSB in solution is strongly fluorescent, but its nanoparticles show weak emission[15,16] like the case of DPST.[9] As UV absorption spectra of PPB nanoparticles are blue-shifted relative to their properties in solution, the observed strong emission in the solid state makes PPB an outstanding exception to a well-established rule based on the molecular exciton model.

To improve our understanding of this atypical phenomenon, we have investigated the dynamics of relaxation from excited states and undertaken structural identification of free PPB and its nanoparticles using these techniques: field-emission scanning electron microscopy (SEM), femtosecond (fs) and picosecond (ps) time-resolved fluorescence dynamics, and X-ray diffraction (XRD). The nanoparticle samples were prepared according to a reprecipitation method in solutions of water and THF.[7a] Two emissive states in PPB nanoparticles were identified in the ps fluorescence transients and confirmed through powder XRD measurements, implying two distinct packing structures. Measurements of the dynamics of femtosecond fluorescence have demonstrated the significance of molecular geometry that affects the relaxation dynamics in the excited state of the free molecule: efficient deactivation of isomerization in PPB was observed because the twisted nature of the geometry accelerates a rotational nonradiative process. Through a combination of results from versatile techniques applied in our work, we conclude that emission from PPB nanoparticles enhanced relative to its THF solution reflects a geometrical change from a twisted conformation to a nearly planar one so as to form a herringbone-type aggregation with an edge-to-face feature shown in the structure of PPB in a single crystal.

Results and Discussion

Formation of PPB Nanoparticles. PPB nanoparticles in a series with varied volume fractions of water, viz. 0, 50, 55, 60, 65, 70, 75, and 80%, were prepared according to a simple reprecipitation method with THF as solvent. The nanoparticle suspension in the mixed solution appeared turbid when the volume fraction of added water exceeded 60%. The color of solutions deepened on increase of the volume fraction of water from 65 to 80%, and the size of nanoparticles increased with increased volume fraction of added water. In four parts, Figure 1 presents SEM photographs of PPB nanoparticles with average particle size varying with water volume fraction of the solutions: (a) 50 nm at 65%, (b) 150 nm at 70%, (c) 300 nm at 75%, and (d) ~1 μm at 80%. According to the evidence shown in Figure 1, the free molecules in the solution begin to aggregate at 65% volume fraction of water addition. Spherically shaped particles were formed initially as the superior solvent THF was replaced by the inferior solvent water and dispersed in bulk water. The observed spherical shape of the nanoparticles likely results from minimization of interfacial energies between PPB and water molecules.[10] As the proportion of added water became greater than 65%, the molecules aggregated to larger structures with some germs of crystallization, and the size of PPB nanoparticles increased greatly. This size-dependent feature indicates that nanocrystallization of PPB proceeds as the volume fraction of water in the solution increases because the water-insoluble PPB molecules aggregate at large water fractions. This formation of PPB nanoparticles with particle size controlled through the proportion of added water is a feature similar to that reported in the cases of PDDP,[8a] DPP,[8b] and DAP[8c] for nanoparticles with size in the range 20−310 nm. When the volume fraction of added water was increased to 80%, extraordinarily large particles (size ~1 μm) were found, and their shape became rectangular (Figure 1d). This formation of rectangular microparticles in 80% solution likely reflects a competition between anisotropic growth and spherical aggregation, similar to a case involving the one-dimensional nanostructures of *p*-BSP in mixtures of water and THF.[10] The size-dependent optical properties of PPB nanoparticles differ from those reported previously,[8,10] as we discuss hereunder.

Steady-State Absorption/Emission Spectra. UV−visible absorption spectra and the corresponding emission spectra of

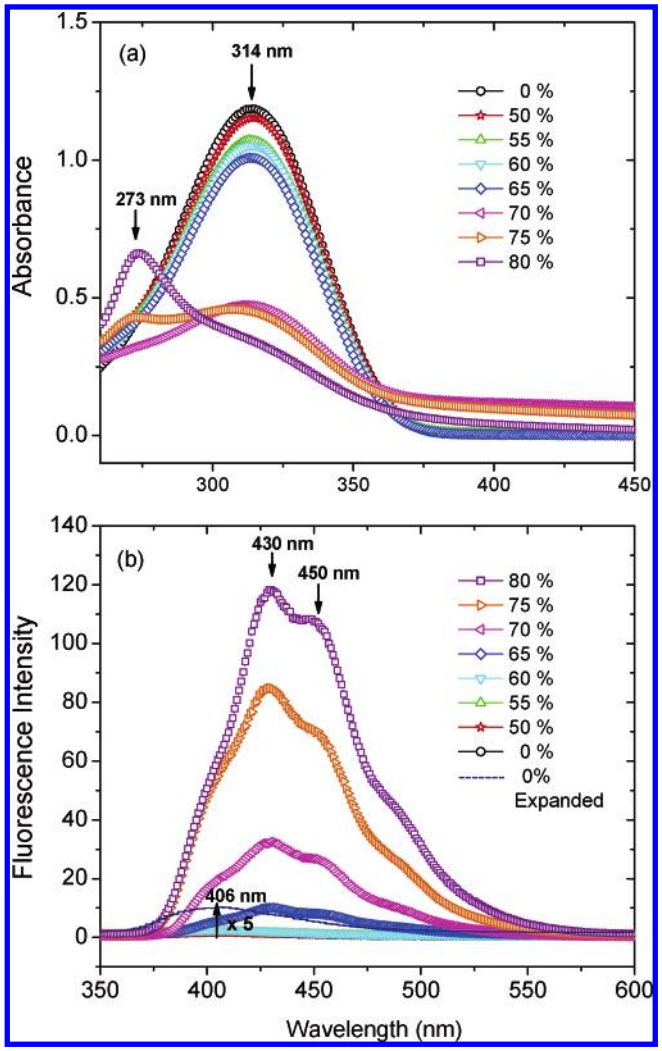

Figure 2. (a) UV−Vis absorption spectra of PPB showing the variation of absorbance with proportions of water and THF as indicated. (b) PL spectra of PPB showing the variation of fluorescent intensity of various mixtures of water and THF as indicated.

PPB with various volume fractions of added water are shown in Figure 2, parts a and b, respectively. The UV−vis spectra (Figure 2a) feature strong absorption with a maximum at 314 nm in solutions of 0−65% water volume fraction. At 70% solution, the absorbance at 314 nm decreases greatly, and a shoulder appears on the blue side of the feature. An additional absorption at 273 nm appears at 75% solution and becomes more pronounced at 80% solution. With the increase of water volume fraction beyond 70%, the notably decreased absorbance at 314 nm accompanying another absorption building at 273 nm implies the formation of PPB nanoparticles at those large volume fractions of added water. The blue-shifted nature of this UV−vis absorption of PPB nanoparticles resembles that observed for DPST[9] and DSB,[15,16] for which a substantially decreased emission intensity was reported on formation of nanoparticles. In contrast, we observed a greatly enhanced fluorescent emission of PPB nanoparticles, of which details follow.

Emission of PPB at 0−60% water volume fraction was barely detectable, indicating the almost nonfluorescent nature of free PPB molecules in dilute solution. The emission spectrum for a solution in THF features a continuous broad band with a maximum near 405 nm, as shown in Figure 2b, with 5-fold enlargement; all other emission spectra with a water volume fraction less than 60% have similar shape and intensity. On formation of PPB nanoparticles with added water above a 60% volume fraction, two new spectral features are worthy of mention for comparison with the emission spectrum of PPB in THF solution. First, emission spectra of PPB for a volume fraction of water between 65 and 80% are distinctly shifted to a greater wavelength (maximum near 430 nm) with an evident vibrational structure. Second, although the observed red-shifted emission spectra all had a similar shape, a substantially enhanced intensity was found for spectra of PPB in 65−80% solutions. As the nanoparticles became larger for volume fractions of added water above 65%, the emission became more intense (Figure 2b). Because this observed intensity systematically increases as a function of volume fraction of added water, we conclude that formation of PPB nanoparticles produces this enhanced emission: the larger the particle is, the more intense the emission becomes.

This observed phenomenon of enhanced fluorescence of PPB nanoparticles resembles that of CN-MBE nanoparticles;[9] both intra- and intermolecular effects have been reported to explain this fluorescence enhancement.[9,10] An intramolecular effect generally implies that free molecules with a twisted conformation in solution undergo efficient relaxation via a nonradiative channel, whereas molecules in planar conformations in the solid state suppress such a deactivation channel. An intermolecular effect arises from interactions between molecules when molecular aggregation becomes significant; this effect depends strongly on the geometry of the packing structure. According to a molecular exciton model,[14] aggregations of two types are involved: H-aggregates tend to accelerate nonradiative relaxation because of strong π-stacking interactions in the parallel aligned structure; in contrast, J-aggregates impede the nonradiative process for molecules arranged in a head-to-tail direction. In the case of CN-MBE, an enhanced emission was attributed to the combined effects of intramolecular planarity and aggregate formation of J-type in nanoparticles because a red-shift in the UV absorption spectra was observed.[9] In our case, UV spectra of PPB nanoparticles show a distinct blue-shift (Figure 2a), which typically indicates formation of H-type aggregates.[14] Our observation of enhanced fluorescence shown in Figure 2b is inexplicable as a typical H-type aggregation as reported for DPST[9] and DSB.[15] To provide an understanding of the mechanism of emission enhancement of PPB nanoparticles, we present further experimental evidence.

Picosecond Relaxation Dynamics of PPB Nanoparticles. Time-dependent measurements of PPB in various mixed solutions in water and THF were performed using time-correlated single-photon counting (TCSPC) with excitation at $\lambda_{ex} =$ 310 nm; typical results ($\lambda_{fl} =$ 420 nm) are shown in Figure 3. The fluorescence decay profiles (transients) of PPB in 0−60% water volume fractions are all characterized exclusively by a sharp spike (the transients for 50, 55, and 60% solutions, not shown in Figure 3, are identical to that of THF solution); the corresponding kinetics could not be determined because of limited temporal resolution of the instrument response (~30 ps). However, the transient at the 65% solution contains two major parts: one part shows a rapid decay with the corresponding kinetics being instrument-limited; the other part shows a slow-decay character with a decay coefficient on a nanosecond time scale (see inset in Figure 3). At 70% volume fraction of water, the slow-decay part is a major component of the transient. With addition of water to volume fractions 75% and 80%, the contribution of the rapid decay became negligible and that of the slow decay became dominant in the transients. These observations indicate that formation of PPB nanoparticles led to formation of new components (the slow-decay part) in the

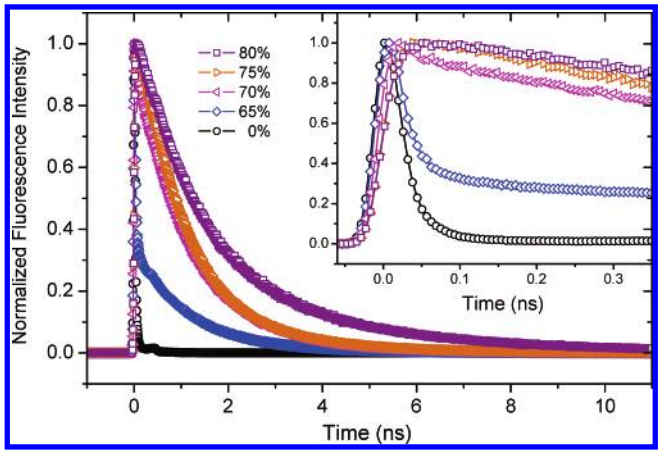

Figure 3. Picosecond fluorescent transients of PPB obtained on excitation at $\lambda_{ex} = 310$ nm and probing at $\lambda_{fl} = 420$ nm for various mixtures of water and THF as indicated. Inset: corresponding transients on a subnanosecond scale.

SCHEME 1: A Dual-Emissive Kinetic Model

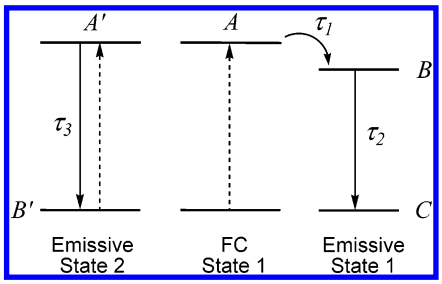

fluorescence transients with much greater lifetimes of the excited state; the larger the nanoparticle is, the more significant the slow-decay part becomes. This feature is consistent with intensity enhancement shown in steady-state fluorescence spectra (Figure 2b).

Because the rapid-decay part of the transients shown for 0−60% solutions arose from the contribution of free PPB molecules (investigated with a femtosecond technique discussed below), we focus on discussion of kinetic data of PPB nanoparticles obtained from the 65−80% solutions. Figures 4a−d show four typical transients for PPB in 65, 70, 75, and 80% solutions, respectively, with excitation at $\lambda_{ex} = 310$ nm and fluorescence observed at $\lambda_{fl} = 480$ nm. All transients show a complicated kinetic feature that is poorly explicable with only a single exponential decay function. As the transients clearly feature a rising character, a simple consecutive kinetic model, $A \xrightarrow{\tau_1} B \xrightarrow{\tau_2} C$, is appropriate in fitting the curves. According to this kinetic model, A represents the initial Franck−Condon (FC) state upon excitation, B denotes a "relaxed" excited state of PPB nanoparticles (emissive state), and C denotes the ground state of nanoparticles (dark state). Hence the FC state decays with a time coefficient τ_1, whereas the emissive state builds up in τ_1 and then decays to the dark state in τ_2. This kinetic model is consistent with the dual-state model utilized in fitting kinetic data for DSB aggregates, for which A represents the intrinsic excitonic state and B denotes a low-energy "defect" state.[17] Even though this kinetic model is capable of describing the rising feature of the transients, the fitting quality of the decay part was unsatisfactory (see Supporting Information for the comparison). To remedy this problem, we added another component, A', with another decay coefficient τ_3 parallel to the consecutive kinetic model, as shown in Scheme 1. In this case, A' represents another emissive state of PPB nanoparticles, of which the structure might differ from that of component B. On the basis of the kinetic model shown in Scheme 1, all transients of 70−80% solutions are satisfactorily described. For the 65% solution, the fits were even more complicated than for the others because the transients at 65% contain a significant contribution from the free species (the spike signal), which smears the important kinetic feature at early times (e.g., Figure 4a). As a result, the slow part of the transients at 65% solution was fitted using only a simple consecutive model, with reasonable results. All fitted parameters are summarized in Table 1; detailed results for these fits are found in Supporting Information.

Figures 5a, b, and c show three fitted time coefficients as a function of fluorescence wavelength (λ_{fl}) for the 65−80% solutions. The values of τ_1 are independent of particle size, but the τ_2 and τ_3 values show a size-dependent feature on lifetimes. In particular, the lifetimes of PPB in the 80% solution are substantially greater than those for 65−75% solutions, reflecting the observed notable change of particle size and shape from 75% to 80% solutions (Figure 1). We found also that the transients of a bulk single crystal of PPB involve no rising character; they can be well fitted with a single-exponential decay to a minute offset (see Supporting Information). We thus consider τ_3 of nanoparticles of PPB to be comparable with the fitted decay coefficient of its bulk crystal shown as a dashed curve in Figure 5c. The τ_3 for the 80% solution matches the decay coefficient of the single crystal with a lifetime in the range 1−2 ns, indicating a similarity between emissive state 2 in PPB aggregates (Scheme 1) and the emissive state of PPB bulk crystal. PPB aggregates in emissive state 1 were produced from the initial FC state with a rise time τ_1 and then decay with τ_2; this feature resembles that of DSB aggregates,[17] for which the observed biexponential fluorescent decays were modeled with two coupled excited states via energy transfer from the excitonic state to the "defect" state. In our case, we regard the emissive state 1 (with decay coefficient τ_2) as a state of lower energy because its contribution becomes a major part of the transients at greater λ_{fl} (Table 1). To provide structural information for the observed two emissive states, we performed X-ray diffraction experiments based on nanoparticles of PPB in 65−80% solutions.

Molecular Structures of PPB in Solid State and in Solution. The powder XRD pattern of a bulk PPB sample is shown in Figure 6a. The appearance of strong reflections for each [00l] plane indicates a strongly preferred orientation due to the plate shape of the crystal, consistent with the calculated powder pattern when the effect of preferred orientation along [00l] planes is taken into account (see Supporting Information). Powder XRD patterns of nanoparticles formed from varied water addition (65−80%) are shown in Figure 6b. In the 2θ range 6−15°, two diffraction features at $2\theta = 9.6°$ and 14.5° correspond to [004] and [006] diffraction planes, respectively, of bulk materials. A further diffraction feature at $2\theta = 7.3°$ ($d = 1.22$ nm) was clearly observed in XRD data of all 65−80% samples. Because the morphology of a crystalline sample affects also the diffraction intensity, the diffraction intensity at $2\theta = 7.3°$ shows no clear correlation for samples of varied water addition. This additional feature indicates that PPB molecules arrange in three-dimensional packing of a new type when nanoparticles are formed. The presence of diffraction features at both $2\theta = 7.3°$ and $2\theta = 9.6°$ and 14.5° in the 65−80% samples indicates that water-induced PPB nanoparticles contain PPB in long-range packing structures of two types; one is the same as the bulk material described below, whereas the other is not yet identified. These powder XRD results confirm that two packing structures are involved in PPB nanoparticles,

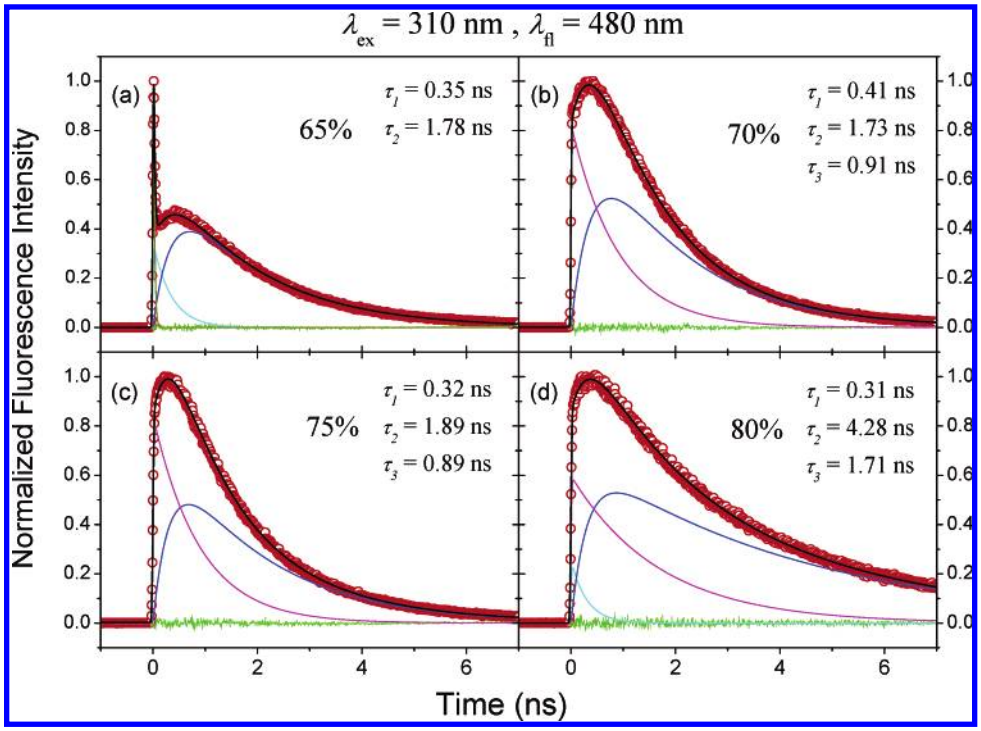

Figure 4. Picosecond fluorescent transients of PPB obtained on excitation at $\lambda_{ex} = 310$ nm and probing at $\lambda_{fl} = 480$ nm for water volume fractions, (a) 65%, (b) 70%, (c) 75%, and (d) 80%. The data were fitted according to the dual-emissive consecutive kinetic model (Scheme 1) detailed in the text with convolution of the instrument response. The solid black curves are theoretical fits with residues shown as green traces; the cyan, blue, and magenta curves under each transient are deconvoluted components corresponding to *A*, *B*, and *A*′, respectively.

TABLE 1: Fitted Time Coefficients of PPB in Various Volume Fractions of Water/THF solution at $\lambda_{ex} = 310$ nm[a,b]

	390 nm				420 nm				450 nm			
λ_{fl}	65%	70%	75%	80%	65%	70%	75%	80%	65%	70%	75%	80%
τ_1 (ns)	0.31 (0.04)	0.05 (0.19)	0.13 (0.25)	0.09 (0.26)	0.26 (0.14)	0.30 (0.08)	0.22 (0.06)	0.23 (0.15)	0.26 (0.16)	0.39 (0)	0.29 (0)	0.23 (0.18)
τ_2 (ns)	1.00 (0.02)	1.48 (0.08)	1.61 (0.17)	2.30 (0.19)	1.26 (0.10)	1.79 (0.16)	2.04 (0.17)	3.45 (0.23)	1.66 (0.19)	1.78 (0.35)	2.00 (0.31)	4.03 (0.35)
τ_3 (ns)		0.68 (0.19)	0.72 (0.58)	0.94 (0.55)		0.87 (0.60)	0.88 (0.77)	1.16 (0.62)		0.92 (0.65)	0.92 (0.69)	1.45 (0.47)
τ (ns)[c]	0.02 (0.94)	0.01 (0.54)			0.02 (0.76)	0.03 (0.16)			0.02 (0.65)			

	480 nm				510 nm				540 nm			
λ_{fl}	65%	70%	75%	80%	65%	70%	75%	80%	65%	70%	75%	80%
τ_1 (ns)	0.35 (0.14)	0.41 (0)	0.32 (0)	0.31 (0.17)	0.39 (0.10)	0.41 (0)	0.32 (0)	0.36 (0.13)	0.40 (0.07)	0.45 (0)	0.32 (0)	0.42 (0)
τ_2 (ns)	1.78 (0.23)	1.73 (0.50)	1.89 (0.45)	4.28 (0.43)	1.86 (0.22)	1.69 (0.59)	1.87 (0.54)	4.43 (0.49)	1.92 (0.18)	1.68 (0.63)	1.86 (0.62)	5.04 (0.48)
τ_3 (ns)		0.91 (0.50)	0.89 (0.55)	1.71 (0.40)		0.88 (0.41)	0.92 (0.46)	2.07 (0.38)		0.88 (0.37)	0.92 (0.38)	2.52 (0.52)
τ (ns)[c]	0.02 (0.63)				0.02 (0.68)				0.02 (0.75)			

[a] The numbers in bracket are the relative amplitudes; the value was set to zero if the contribution of the component was too small to be sensitive to the fit. [b] All parameters were obtained according to the kinetic model shown in Scheme 1 except the transients of 65% solution via a simple consecutive model. [c] Time coefficients due to free PPB in solution are instrument limited (<30 ps).

consistent with results obtained from picosecond time-resolved experiments in which two emissive states are observed (Figure 4).

Single crystals of PPB suitable for XRD measurements were obtained on slow evaporation of its THF solution. Figure 7 shows crystal structures of plate-shaped PPB in three directions. There are four independent PPB molecules in a unit cell. The packing of PPB molecules along the *a*-axis shows a structure of herringbone type (Figure 7a); such a molecular packing feature is similar to that of chemically related compounds, e.g., DSB[18] and other OPV.[19] For each PPB molecule, the ethene moieties are parallel to the *a*-axis and twisted with respect to the benzene rings with an average torsional angle 31°. The direction of the ethene moieties in a PPB molecule is shown in Figure 7b. For each PPB molecule, three benzene rings are connected through two ethene moieties; each ethene moiety connects two benzene rings in a trans conformation. The central benzene ring connects two phenyl groups via the ethene moiety in 1,4-positions. The ethene moieties on 1,4-sites of the central phenyl ring appear to point to the same side. In three-dimensional packing, PPB molecules along the *c*-axis are correlated with a 2_1 symmetry, which causes the methyl groups

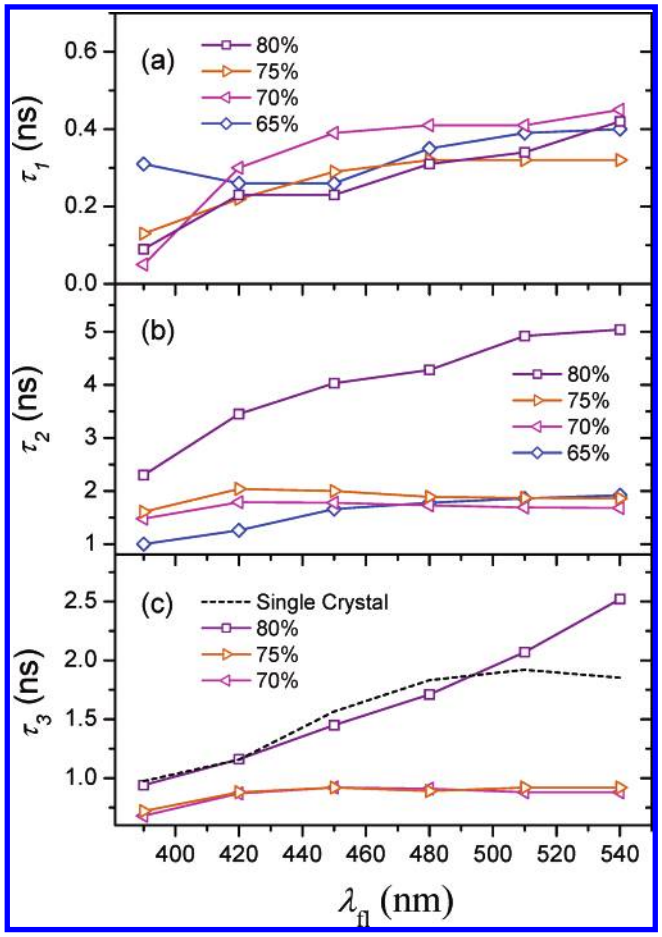

Figure 5. Three fitted temporal coefficients of PPB, (a) τ_1, (b) τ_2, and (c) τ_3, as a function of fluorescence wavelength for various mixtures of water and THF as indicated; the corresponding fitted parameters are summarized in Table 1. The dashed curve shown in (c) represents the wavelength-dependent single-exponential-decay coefficient of the PPB single crystal.

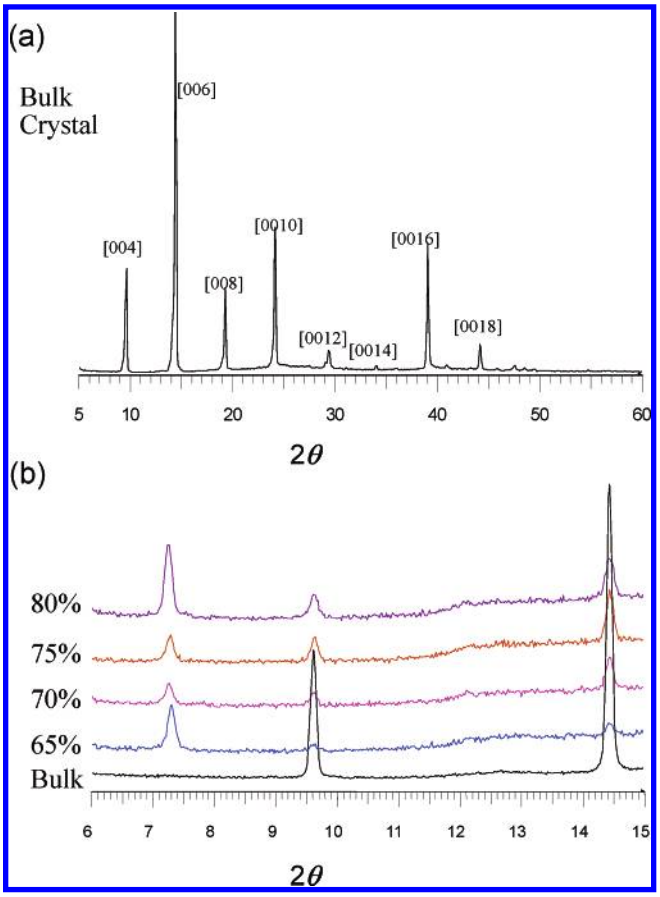

Figure 6. (a) Powder XRD pattern of PPB bulk material. (b) Powder XRD patterns of PPB nanoparticles from various mixtures of water and THF as indicated.

in adjacent PPB molecules to point in opposite directions (Figure 7b). The intermolecular packing of PPB molecules is shown in Figure 7c for a single layer of PPB molecules on the *ab* plane; the structure is rotated by 7° along the *a*-axis to make the PPB molecule nearly perpendicular to the plane. This structural model has been used in calculating the XRD powder pattern of PPB. The simulated pattern is consistent with the result from the powder XRD experiment of bulk PPB material when the effect of preferred orientation on the [00l] direction is applied.

Each ethene moiety is parallel to the *a*-axis and twisted with respect to the benzene rings. As the ethene moiety in this four-PPB unit is aligned in the same direction (*a*-axis), the dipole moment for PPB in each layer aligns in the same direction but opposite in the adjacent layer. Moreover, the two-dimensional packing of a PPB molecule on the *ab* plane is near the edge-to-face interactions of a 2 × 2 pinwheel pattern, similar to DSB.[20] In that case, the molecular skeleton of the DSB unit in the crystal structure is completely planar. Theoretical simulations indicate that the rate of radiative decay of DSB in a pinwheel is one-quarter that of a single molecule.[20] For PPB, we observed strong fluorescence from the aggregates, likely reflecting the pinwheel packing of PPB being affected to some extent by steric interference of methyl groups and by the "out-of-plane" nature of the ethene moiety with respect to the benzene rings (Figure 7c). The edge-to-face interactions in the pinwheel of PPB thus become more significant than those in DSB, so enhancement of fluorescence was observed from PPB aggregates, whereas quenching of fluorescence was observed for DSB aggregates.[15,16] Theoretical calculations are required to illuminate this anomalous optical behavior observed between PPB and DSB aggregates.

Optimized structures of isolated PPB and DSB molecules are shown in Figure 8, parts a and b, respectively. The free DSB molecule has a planar geometry, with all atoms located in the same symmetry plane, but the free PPB molecule has a nonplanar structure with one end benzene ring twisted from the molecular plane by ~80°. The structure of the free PPB molecule (Figure 8a) differs markedly from that in a single crystal (see Figure 7, parts b and c), in which three benzene rings in PPB align parallel to a symmetry plane similar to the planar geometry of the free DSB molecule (Figure 8b). A correlation of emission intensities with molecular structures of PPB between solution and solid phases has been discovered: the twisted conformation of a free PPB molecule is essentially nonfluorescent in dilute solution, whereas the planar geometry of the three benzene rings in the PPB unit cell of aggregates produces strong emission in the solid state. The reason for this observed enhancement of emission from solutions of 65−80% water seems to be the conformational change of PPB molecules when aggregating to nano- or micro-size particles. To understand further a mechanism for molecular geometry affecting the excited-state relaxation dynamics that causes a great variation in emission intensity, we performed femtosecond fluorescence up-conversion measurements for isolated PPB and DSB molecules dissolved in dilute THF solution and for their nanoparticles formed in 75% solution.

Femtosecond Relaxation Dynamics of PPB and DSB. The structures of isolated PPB and DSB molecules are intrinsically

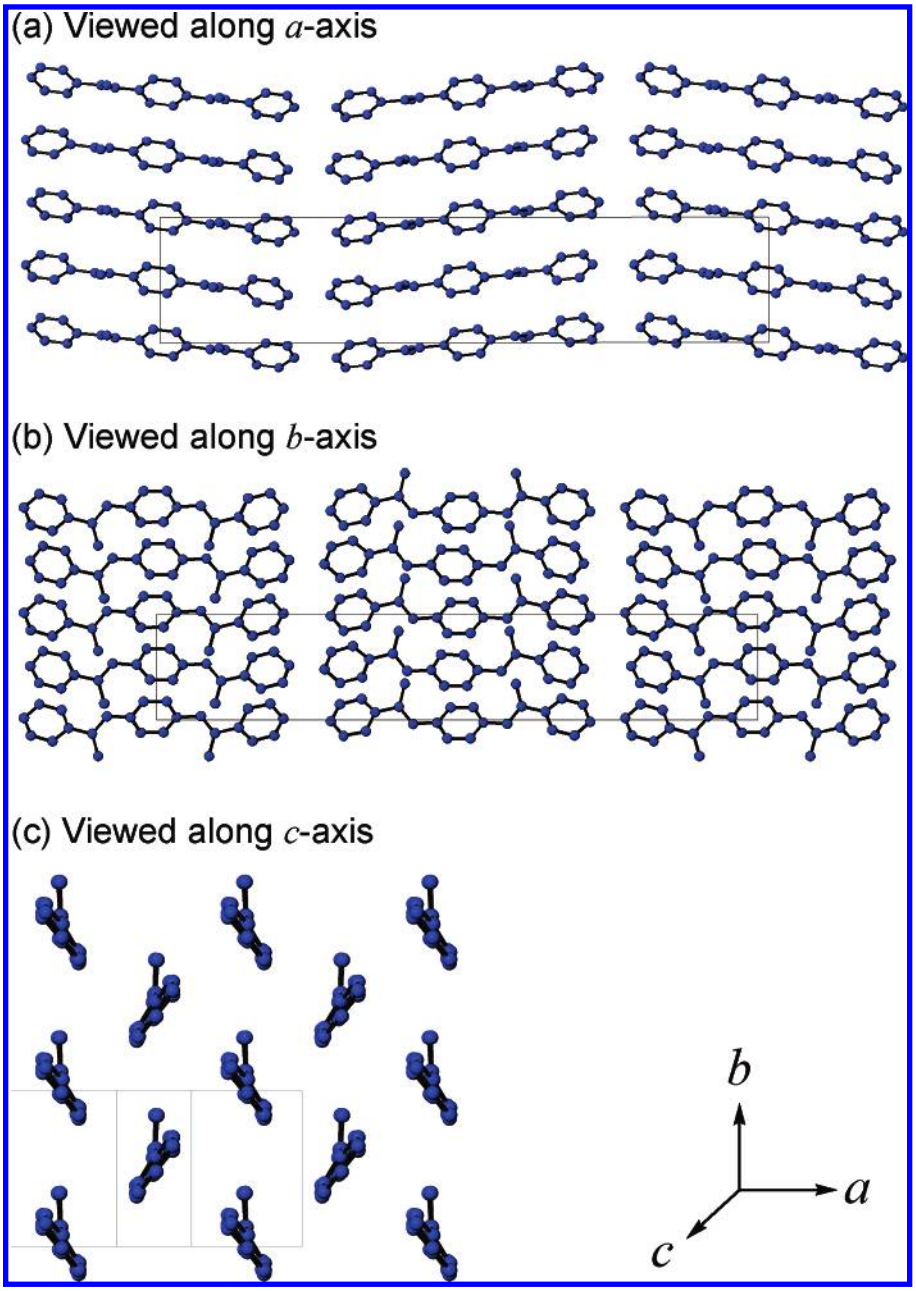

Figure 7. Projection of the structure of PPB viewed along (a) [001], (b) [010], and (c) [001] directions. Blue circles: C. Hydrogen atoms are omitted for clarity.

different (Figure 8). The twisted geometry of PPB might reflect a balance between strong hyperconjugation of methyl groups with individual benzene rings and a long-range conjugation across all benzene rings. Consistent with this idea, we observed that PPB in dilute solution is almost nonfluorescent, but free DSB molecules produce strong emission[15,16] like PPB aggregates. Figure 9, parts a and b show two typical fluorescence transients taken at $\lambda_{ex} = 360$ nm and $\lambda_{fl} = 450$ nm for PPB and DSB in THF, respectively. The rapid kinetics of PPB in THF solution, previously undetermined because of limited temporal resolution, have been unraveled in the transients shown in Figure 9a with ~280-fs resolution. The transients were analyzed according to an appropriate kinetic model with convolution of the instrument response function. For PPB, three kinetic components are required to fit the transient, yielding two decay coefficients (1 and 9 ps) with a small offset component persistent on a ps time scale. For DSB, the transient shows no rapid-decay feature, but a reasonable fit of the transient was obtained on including two transient components; one component decays in ~10 ps, whereas the other component rises in ~10 ps and persists on a ps time scale. The contribution of the persistent component to the transient of PPB is minor, whereas it becomes a major part of the transient in DSB. This transient property eliminates observable emission of the former, whereas strong emission was observed for the latter. The contribution of the ~1-ps component is significant in the transient of PPB but negligible in the transient of DSB. The rapid ps component unambiguously shown in the transient of PPB, therefore, plays an important role in diminishing the contribution of the slow ns component to the fluorescent transient. As a free PPB molecule has a twisted geometry, whereas the free DSB molecule is planar (Figure 8), a correlation between molecular structure and the observed relaxation dynamics evidently exists and is discussed in the following.

According to results obtained for the isolated *trans*-stilbene molecule, which is planar with two benzene rings connected

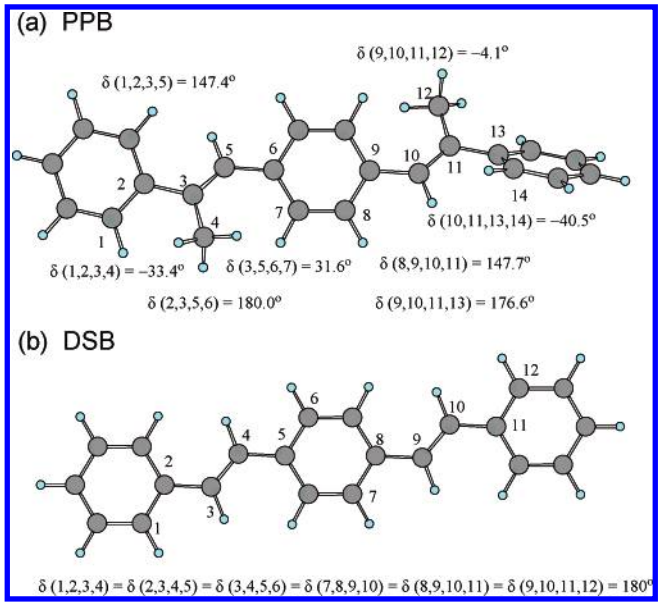

Figure 8. Ground-state structure of the isolated molecule (a) PPB and (b) DSB optimized at the B3LYP/6-31G(d) level of theory; relevant torsional angles are indicated.

through an ethene moiety in a trans form, the nonradiative process in the first singlet excited state (S_1) is governed by isomerization, according to the ethene twisting reaction coordinate, with an energy barrier only 14.2 kJ mol^{-1}.[21] Taking into consideration the photoisomerization mechanism of *trans*-stilbene in relation to systems in the present work, we speculate that the observed ps relaxation in nonplanar PPB is the result of crossing a small energy barrier along the C═C rotation channel on the S_1 surface, for which an efficient $S_1 \rightarrow S_0$ internal conversion occurs at the perpendicularly twisted conformation (the so-called "phantom state" in the stilbene system)[21] so that the ns component is difficult to observe. For the planar DSB molecule in solution, the ps nonradiative deactivation through this C═C twisting motion was not observed, likely reflecting a large energy barrier along the isomerization channel in the S_1 state. Solvent-induced vibrational relaxation (VR) also competes with a barrier-crossing deactivation, which produces an observed ~10-ps component in both systems. Because deactivation through isomerization is much slower than VR in DSB, the electronically excited molecules preferentially lose their vibrational energy in the S_1 state so that electronic relaxation occurs from only a "cold" S_1 state, hence producing the prominent ns component observed for DSB.

Figure 10, parts a and b show two typical fluorescence transients taken at $\lambda_{ex} = 360$ nm and $\lambda_{fl} = 450$ nm for PPB and DSB nanoparticles produced from the 75% solutions, respectively. Both transients are satisfactorily described with two components: the first component decays in ~45 ps, whereas the second component persists in the observed 100-ps region. The 45-ps component shown in the fs transient of the PPB nanoparticles, previously unresolved in the transients obtained using the TCSPC method with much worse temporal resolution, thus reflects the initial phase of relaxation in nanoparticles. Because the nuclear motions are restricted in nanoparticles, the observed 45-ps component in both systems might be due to a nonradiative deactivation process through intermolecular interactions involving π-stacking of the carbon backbones. For DSB, the observed 43-ps component becomes a major part of the transient because of its tighter coplanar arrangement with stronger π-overlap in the solid state,[18−20] which significantly

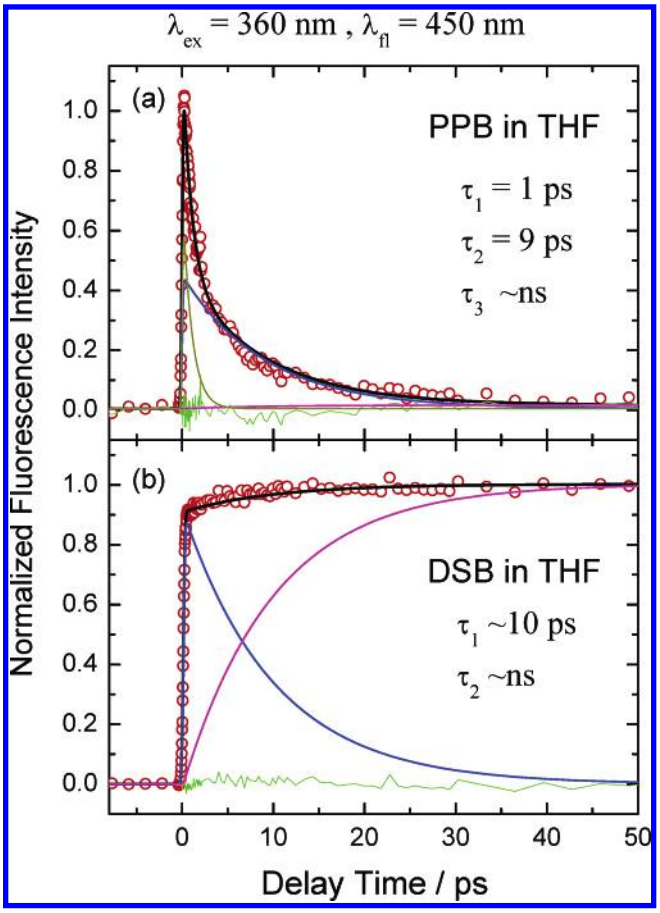

Figure 9. Femtosecond fluorescent transients of (a) PPB and (b) DSB in pure THF obtained from $\lambda_{ex} = 360$ nm and $\lambda_{fl} = 450$ nm. The transient of PPB was fitted according to a combined consecutive kinetic model, $A' \xrightarrow{\tau_1} B'$ and $A \xrightarrow{\tau_2} B \xrightarrow{\tau_3} C$, whereas that of DSB with a simple consecutive model, $A \xrightarrow{\tau_1} B \xrightarrow{\tau_2} C$. The solid black curves are theoretical fits with residues shown as green traces; the blue and magenta curves under each transient are deconvoluted components corresponding to *A* and *B*, respectively; a dark yellow curve shown under the transient of PPB represents *A*′.

decreases the contribution of the ns component for the much smaller fluorescence quantum yield observed for nanoparticles ($\Phi_F < 0.1$) than for DSB in solution ($\Phi_F = 0.9$).[15] For PPB, in contrast, the 45-ps component becomes a minor part of the transient because the packing structure of PPB in the solid state is looser than that of DSB because of the hindrance of the methyl groups of the former. The rapid-decay component (1 ps) was completely absent in the fs transient of PPB nanoparticles, indicating the significance of the confined geometry of nanoparticles in suppressing an efficient nonradiative torsional deactivation and retaining the amplitude of the ns component for the enhanced emission observed in the solid phase.

Concluding Remarks

In the present work, we report optical properties of PPB nanoparticles dependent on their size; these particles were prepared by reprecipitation in solutions of water and THF at various volume fractions and are characterized by SEM, XRD, picosecond, and femtosecond time-resolved spectral methods. We observed strong emission from PPB nanoparticles, but emission of free PPB in dilute solution was scarcely detectable. Furthermore, the fluorescent intensity of these nanoparticles increases with their size. Measurements of femtosecond fluo-

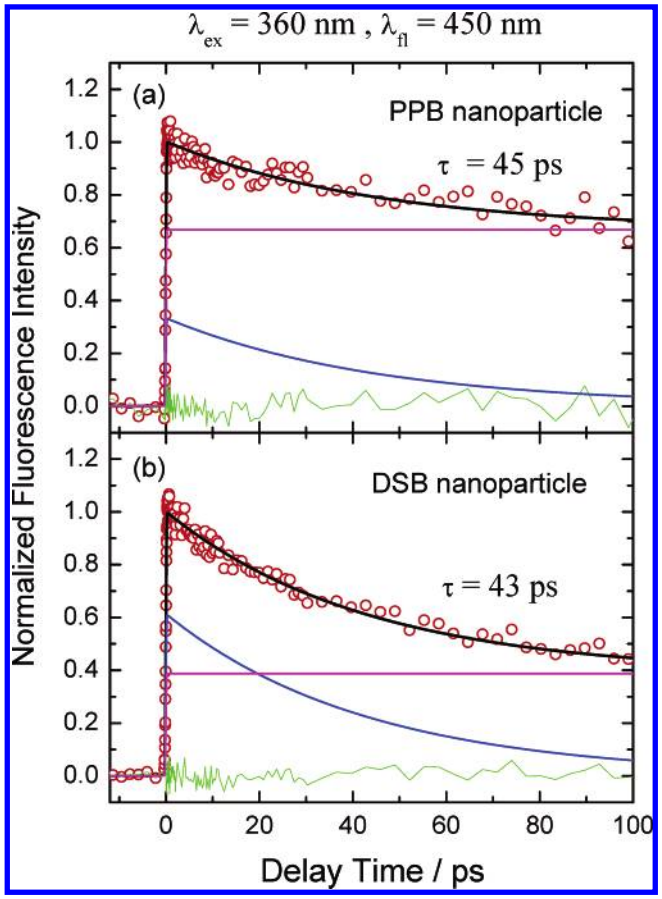

Figure 10. Femtosecond fluorescent transients of (a) PPB and (b) DSB in 75% solutions obtained from $\lambda_{ex} = 360$ nm and $\lambda_{fl} = 450$ nm. The transients were fitted by a parallel kinetic model with two components: the first component (blue curves) decays in ~45 ps, but the second component (magenta curves) persists in the 100-ps region.

rescence indicate that intramolecular nonradiative deactivation through torsional motions is efficient in PPB solution but inactive in DSB solution; intermolecular nonradiative deactivation through $\pi-\pi$ interactions of carbon backbones is more efficient in DSB nanoparticles than in PPB nanoparticles. Such disparate dynamical behavior is inferred to reflect the dissimilar structures of PPB and DSB molecules in dilute solution and in nanoparticles. In this manner, we rationalize the nonfluorescent nature of the twisted PPB molecule in dilute solution and establish the concept that molecular planarity, geometrical rigidity, and loose packing produce strong fluorescent emission in PPB nanoparticles.

A nearly planar geometry of molecules of PPB in the unit cell of a single crystal is confirmed by our XRD measurements. Moreover, powder XRD experiments demonstrate that two packing structures are involved in PPB nanocrystals: one forms aggregates according to a herringbone-type arrangement as observed in a single crystal, whereas the other is not yet determined. This dual-aggregate feature of nanoparticles is reflected in the biexponential kinetics according to the picosecond time-resolved experiments for two emissive states observed: one features a single-exponential decay as observed for the single crystal, whereas the other shows a rising feature associated with the unknown structure detected from the XRD data. The observed induction period of the emissive state likely reflects an involvement of solvent molecules inside the nanocrystal of the unknown structure.

In summary, PPB exhibits weak emission in dilute solution but blue-shifted absorption and anomalously strong emission in nanoparticle aggregates. We present experimental evidence that enhanced emission of nanoparticles is due to the combined effects of a planar conformation and the formation of herringbone-type aggregates with an edge-to-face feature shown in the structure of PPB in a single crystal.

Experiments

Materials. PPB was synthesized by Heck coupling.[22] A mixture of α-methylstyrene (2.5 g, 25.4 mmol), 1,4-dibromobenzene (2.0 g, 8.4 mmol), palladium(II) acetate (0.04 g, 0.16 mmol), tri-(ortho-tolylphosphine) (0.10 g, 0.33 mmol), and triethylamine (4.92 g, 48.78 mmol) was prepared in a thick-walled screw-capped glass tube. The tube was capped under argon and heated for 24 h at 120 °C. After cooling, the mixture was extracted with ethyl acetate; the organic layer was washed with saturated NaCl, water, and dry $MgSO_4$. After filtration and evaporation of the solvent, the solid crude was recrystallized from hexane to produce fine transparent crystals (yield, 65%). ^{1}H NMR (300 MHz, $CDCl_3$): $\delta = 7.51-7.54$ (m, 4H; Ar−H), 7.34−7.39 (m, 8H; Ar−H), 7.27−7.30 (m, 2H; Ar−H), 6.82−6.83 (d, 2H; vinyl), 2.32 (d, 6H; $-CH_3$).

Formation of Nanoparticles. PPB nanoparticles were prepared by a simple reprecipitation method.[7a] Water served as a precipitating solvent for PPB in THF. Water was added in volume fractions up to 80%, with vigorous stirring at 296 K. Distilled water and THF were filtered with a membrane filter (pore size 0.2 μm). In all samples (mixtures), the concentration of chromophore (2.9×10^{-5} mol L^{-1}) was constant after addition of distilled water. After 60% volume fraction of water addition, aggregation of PPB in the mixed solution produced nanosize particles. These suspensions were homogeneous and stable, even after four months. Samples for powder diffraction and SEM tests were prepared as follows: the sample was dropped onto a glass substrate (for powder XRD) or a carbon tape (for SEM) and dried near 296 K. To accumulate a sufficient sample, we repeated this process several times.

Steady-State Spectral Measurements. ^{1}H NMR spectra were recorded (Unity-300 spectrometer at 300 MHz) in $CDCl_3$ solutions. Images were acquired on a field-emission scanning electron microscope (JSM-6500 F, JEOL); to enhance the conductivity of the specimen, a layer of platinum was sputtered (duration 30 s, current 30 mA, pressure 4 Pa). UV−vis absorption spectra (Hewlett-Packard HP8453 spectrometer) and fluorescence spectra (Hitachi F4500 spectrophotometer) were measured in a standard manner.

Time-Resolved Spectral Measurements. *(a) Femtosecond Up-Conversion Measurements.* Femtosecond time-resolved spectra were obtained with a fluorescence optically gated system (FOG100, CDP) in combination with a mode-locked Ti-sapphire laser (Mira 900D, Coherent) pumped with a 10-W Nd:YVO_4 laser (Verdi-V10, Coherent). Details of this experimental setup appear elsewhere.[23] Briefly, the femtosecond laser system generates output pulses with a duration 100−150 fs at a repetition rate of 76 MHz. The fundamental frequency of the laser pulse was tunable over a range of 700−1000 nm; a typical spectral bandwidth, full width at half-maximum (fwhm), measured at 720 nm, was ~8 nm. The frequency of the laser pulse was doubled for excitation (pump). The residual fundamental pulse was used as a probe; a dichroic beam splitter served to separate pump and probe beams. The excitation beam intensity was appropriately attenuated and then focused onto a 1-mm rotating cell containing the sample solution. The fluorescence was collected with a lens pair and focused on a BBO type-I crystal (thickness 0.5 mm). The gate pulse (probe) was

also focused on a BBO crystal for sum frequency generation (SFG). The latter signal was collected with a lens and separated from interference light with an iris, a band-pass filter, and a double monochromator (DH10, Jobin Yvon) in combination, then detected with a photomultiplier (R1527P, Hamamatsu) connected to a computer-controlled photon-counting system. On varying the temporal delay between gate and excitation pulses via a stepping-motor translational stage, we obtained a temporal profile (transient). The polarization between the pump and probe pulses was fixed at the magic-angle condition (54.7°).

(b) Picosecond TCSPC Measurements. Picosecond time-resolved experiments were performed with a TCSPC system (Fluotime 200, PicoQuant). The repetition rate of the laser pulse (output from Mira 900D) was decreased to 4.76 MHz using a pulse picker (9200, Coherent); the frequency was tripled with a harmonic generation system (9300, Coherent). A small portion of the fundamental laser pulse was fed into a fast photodiode (TDA200, PicoQuant) as a reference trigger to synchronize the timing as a signal to initiate the TCSPC system. The excitation laser was focused onto a cuvette (thickness 1 cm) containing a sample solution. Fluorescence emitted at a right angle was collected with a lens pair. The wavelength of fluorescence was selected via a double monochromator (f/3.2, 8 nm/mm dispersion, of subtractive type to correct for distortion of group velocity dispersion). A microchannel plate photomultiplier (R3809U-50, Hamamatsu) served as a photon-counting detector, from which the signal was fed into a computer with a TCSPC module (SPC-630, Becker and Hickl) for data acquisition. With a polarizer, we selected the polarization of the emission with respect to the excitation laser pulse; in all experiments reported here, the polarization was fixed at the magic-angle condition (54.7°). The fwhm of the instrument response function (IRF) was determined to be ~30 ps.

X-ray Crystallography. *(a) Powder XRD Collections.* X-ray powder diffraction data of PPB were collected with a diffractometer (Bruker D8, 40 kV, 40 mA) with Bragg−Brentano geometry, Cu Kα radiation ($\lambda = 0.15406$ nm), and a 40-mm Göbel mirror. For a bulk sample, the powder pattern was scanned over an angular range of 5−60° of 2θ, with an increment of 0.1° (2θ) and a counting duration of 4 s per step. For nanoparticles (from 65 − 80% solutions) and bulk, the pattern was scanned over an angular range 5−16° (2θ), with an increment of 0.02° (2θ) and a counting duration of 10 s per step. The measurements were performed at 296 K.

(b) Single-Crystal XRD Collections. Single crystals of PPB suitable for X-ray diffraction measurements were obtained on slow evaporation of its THF solution. A crystal with an average cubic shape ($0.1 \times 0.1 \times 0.1$ mm^3) was selected under an optical microscope, glued onto a glass fiber, and mounted in a diffractometer (Enraf-Nonius CAD4, Mo K_α radiation with $\lambda = 0.071073$ nm, ω-2θ scan mode). SEARCH procedures were conducted for orientation matrix determination and peak indexing on the basis of 25 observed reflections. An orthorhombic cell was initially found with $a = 0.630(2)$ nm, $b = 0.756(2)$ nm, $c = 3.67(7)$ nm, $V = 1.750(3)$ nm^3. Single-crystal X-ray diffraction data were collected with the use of graphite-monochromatized Mo Kα radiation ($\lambda = 0.71073$ Å) at 298(2) K on a Bruker APEX CCD diffractometer. The distance from crystal to detector was 5.93 cm. Data were collected by a scan of 0.3° in ω in groups of 1315 frames each at ϕ settings 0°, 90°, and 180°, respectively. The exposure time was 60 s frame^{-1}. The 2θ values varied between 3° and 56.5°. The data were corrected for Lorentz and polarization effects. Absorption corrections were based on fitting a function to the empirical transmission surface as sampled by multiple equivalent measurements of numerous reflections [11 375 reflections scanned, 2498 unique ($R_{Int} = 0.018$), 11 071 with $I > 2\sigma(I)$].[24] Diffraction signals obtained from all frames of reciprocal space images were used to determine the unit-cell parameters. The crystal revealed an orthorhombic unit cell ($a = 36.813(3)$ Å, $b = 6.2947(5)$ Å, $c = 7.5555(6)$ Å, $V = 1750.8(2)$ Å^3), and systematic absences indicated a space group $P2_12_12_1$ (No. 19). The structure model was obtained by direct methods and refined by full-matrix least-squares refinement based on F^2 using the SHELXTL5.12 package.[25] All carbon atoms were refined with anisotropic displacement parameters. The positions of hydrogen atoms were obtained from difference Fourier maps and refined with isotropic displacement parameters. Final structure refinements reveal $R1 = 4.3\%$ and $R2 = 10.1\%$.

Computational Methods. The structures of isolated PPB and DSB molecules were determined with density-functional theory (DFT) implemented in the G03 software package.[26] Geometries of molecules in the ground state were optimized at the B3LYP/6-31G(d) level of theory with vibrational frequencies calculated at the same level being all positive numbers.

Acknowledgment. We thank M. C. Lin for many helpful discussions, and acknowledge financial support by the National Science Council of the Republic of China (project contracts 93-2113-M-009-007, 93-2113-M-009-016, and 93-2120-M-009-008 for C.S.L., E.W.G.D., and C.S.H., respectively).

Supporting Information Available: Fluorescence transients with fitted results of the bulk crystal and PPB in 65−80% solutions (five figures) supplement analyzed results summarized in Table 1 and Figure 5; a demonstration of quality of fits between two kinetic models is provided; crystal data for PPB crystal are summarized in Table A1, atomic coordinates are given in Table A2, interatomic distances are shown in Table A3, anisotropic displacement parameters are shown in Table A4, and isotropic displacement parameters are shown in Table A5; the calculated powder XRD pattern of the bulk PPB crystal and the cif file for crystal database are provided. This material is available free of charge via the Internet at http://pubs.acs.org.

References and Notes

(1) Horn, D.; Rieger, J. *Angew. Chem., Int. Ed.* **2001**, *40*, 4330−4361, and references therein.

(2) (a) Forrest, S. *MRS Bull.* **2001**, *26*, 108−112. (b) Alivistos, A. P. *Science* **1996**, *271*, 933−937. (c) Peng, X. G. *J. Am. Chem. Soc.* **1997**, *119*, 7019−7029.

(3) Silinsh, E. A. In *Organic Molecular Crystals: Their Electronic States*; Springer-Verlag: Berlin, 1980.

(4) Yoshikava, H.; Masuhara H. *J. Photochem. Photobiol., C* **2000**, *1*, 57−58.

(5) (a) Chemla, D. S.; Zyss, J. In *Nonlinear Optical Properties of Organic Molecules and Crystals*; Academic Press: Orlando, FL, 1987; Vol. 1. (b) Gehr, R. J.; Boyd, R. W. *Chem. Mater.* **1996**, *8*, 1807−1819.

(6) (a) Oikawa, H.; Kasai, F.; Nakanishi, H. In *Anisotropic Organic Materials*; Glaser, R., Kasizynski, P., Eds.; ACS Symposium Series 798; American Chemical Society: Washington, DC, **2002**; Chapter 12, pp 169−178. (b) He, J. A.; Yang, K.; Kumar, J.; Tripathy, S. K.; Samuelson, L. A.; Oshikiri, T.; Katagi, H.; Kasai H.; Okada S.; Oikawa H.; Nakanishi H. *J. Phys. Chem. B* **1999**, *103*, 11050−11056.

(7) (a) Kasai, H.; Nalwa, H. S.; Oikawa, H.; Okada, S.; Matsuda, H.; Minami, N.; Kakuta, A.; Ono, K.; Mukoh, A.; Nakanishi, H. *Jpn. J. Appl. Phys.* **1992**, *31*, L1132−L1134. (b) Kasai, H.; Kamatani, H.; Okada, S.; Oikawa, H.; Matsuda, H.; Nakanishi, H. *Jpn. J. Appl. Phys.* **1996**, *35*, L221−L223. (c) Onodera, T.; Kasai, H.; Okada S.; Oikawa, H.; Mizuno, K.; Fujitsuka, M.; Ito, O.; Nakanishi, H. *Opt. Mater.* **2002**, *21*, 595−598. (d) Oikawa, H.; Mitsui, T.; Onodera, T.; Kasai, H.; Nakanishi, H.; Sekiguchi, T. *Jpn. J. Appl. Phys., Part 2* **2003**, *42*, L111−L113. (e) Katagi, H.; Kasai, H.; Okada, S.; Oikawa H.; Komatsu, K.; Matsuda, H.; Liu, Z.; Nakanishi, H. *Jpn. J. Appl. Phys.* **1996**, *35*, L1364−L1366. (f) Baba K.; Kasai, H.; Okada, S.; Oikawa, H.; Nakanishi, H. *Opt. Mater.* **2002**, *21*, 591−594.

(g) Takahashi, S.; Miura, H.; Kasai, H.; Okada, S.; Oikawa, H.; Nakanishi, H. *J. Am. Chem. Soc.* **2002**, *124*, 10944−10945.

(8) (a) Fu, H. B.; Yao, J. N. *J. Am. Chem. Soc.* **2001**, *123*, 1434−1439. (b) Fu, H. B.; Loo, B. H.; Xiao, D.; Xie, R.; Ji, X.; Yao, J.; Zhang, B.; Zhang, L. *Angew. Chem., Int. Ed.* **2002**, *41*, 962−865. (c) Xiao, D.; Xi, Lu; Yang, W.; Fu, H.; Shuai, Z.; Fang, Y.; Yao, J. *J. Am. Chem. Soc.* **2003**, *125*, 6740−6745.

(9) An, B.-K.; Kwon, S.-K.; Jung, S.-D.; Park, S.-Y. *J. Am. Chem. Soc.* **2002**, *124*, 14410−14415.

(10) Li, S.; He, L.; Xiong, F.; Li, Y.; Yang, G. *J. Phys. Chem. B* **2004**, *108*, 10887−10892.

(11) Luo, J.; Xie, Z.; Lam, J. W. Y.; Cheng, L.; Chen, H.; Qiu, C.; Kwok, H. S.; Zhan, X.; Liu, Y.; Zhu, D.; Tang, B. Z. *Chem. Commun.* **2001**, 1740−1741.

(12) Deans, R.; Kim, J.; Machacek, M. R.; Swager, T. M. *J. Am. Chem. Soc.* **2000**, *122*, 8565−8566.

(13) Birks, J. B. In *Photophysics of Aromatic Molecules*; Wiley: London, 1970.

(14) Hans K.; Försterling, H.-D. In *Principles of Physical Chemistry, Understanding Molecules, Molecular Assemblies, Supramolecular Machines*; Wiley: New York, 2000.

(15) Oelkrug, D.; Tompert A.; Gierschner, J.; Egelhaaf, H.-J.; Hanack, M.; Hohloch, M.; Steinhuber, E. *J. Phys. Chem. B* **1998**, *102*, 1902−1907.

(16) Egelhaaf, H. J.; Gierschner, J.; Oelkrug, D. *Synth. Met.* **1996**, *83*, 221−226.

(17) Lim, S.-H.; Bjorklund, T. G.; Bardeen, C. J. *J. Phys. Chem. B* **2004**, *108*, 4289−4295.

(18) Wu, C. C.; DeLong M. C.; Vardeny, Z. V.; Ferraris J. P. *Synth. Met.* **2003**, *137*, 939−941.

(19) van Hutten, P. F.; Wildeman, J.; Meetsma, A.; Hadziioannou, G. *J. Am. Chem. Soc.* **1999**, *121*, 5910−5918.

(20) Spano, F. C. *Synth. Met.* **2001**, *116*, 339−342.

(21) Baskin, J. S.; Banares, L.; Zewail, A. H. *J. Phys. Chem.* **1996**, *100*, 11920−11933, and references therein.

(22) Dieck, H. A.; Heck, R. F. *J. Am. Chem. Soc.* **1974**, *96*, 1133−1136.

(23) Lu, Y. C.; Chang, C. W.; Diau, E. W. G. *J. Chin. Chem. Soc.* **2002**, *49*, 693−701.

(24) *SAINT Program*, Version 4; Siemens Analytical X-ray Instruments Inc.: Madison, WI, 1995.

(25) Sheldrick, G. M. *SHELXTL, Structure Determination Programs*, Version 5.12; Siemens Analytical X-ray Instruments Inc.: Madison, WI, 1995.

(26) Frisch, M. J.; Trucks, G. W.; Schlegel, H. B.; Scuseria, G. E.; Robb, M. A.; Cheeseman, J. R.; Montgomery, Jr., J. A.; Vreven, T.; Kudin, K. N.; Burant, J. C.; Millam, J. M.; Iyengar, S. S.; Tomasi, J.; Barone, V.; Mennucci, B.; Cossi, M.; Scalmani, G.; Rega, N.; Petersson, G. A.; Nakatsuji, H.; Hada, M.; Ehara, M.; Toyota, K.; Fukuda, R.; Hasegawa, J.; Ishida, M.; Nakajima, T.; Honda, Y.; Kitao, O.; Nakai, H.; Klene, M.; Li, X.; Knox, J. E.; Hratchian, H. P.; Cross, J. B.; Bakken, V.; Adamo, C.; Jaramillo, J.; Gomperts, R.; Stratmann, R. E.; Yazyev, O.; Austin, A. J.; Cammi, R.; Pomelli, C.; Ochterski, J. W.; Ayala, P. Y.; Morokuma, K.; Voth, G. A.; Salvador, P.; Dannenberg, J. J.; Zakrzewski, V. G.; Dapprich, S.; Daniels, A. D.; Strain, M. C.; Farkas, O.; Malick, D. K.; Rabuck, A. D.; Raghavachari, K.; Foresman, J. B.; Ortiz, J. V.; Cui, Q.; Baboul, A. G.; Clifford, S.; Cioslowski, J.; Stefanov, B. B.; Liu, G.; Liashenko, A.; Piskorz, P.; Komaromi, I.; Martin, R. L.; Fox, D. J.; Keith, T.; Al-Laham, M. A.; Peng, C. Y.; Nanayakkara, A.; Challacombe, M.; Gill, P. M. W.; Johnson, B.; Chen, W.; Wong, M. W.; Gonzalez, C.; Pople, J. A. *Gaussian 03*, Revision B.5; Gaussian, Inc., Wallingford CT, 2004.